Research paper

Nickel nanoparticles embedded in mesopores of AlSBA-15 with a perfect peasecod-like structure: A catalyst with superior sintering resistance and hydrothermal stability for methane dry reforming

Xianhua Zhang[a,1], Li Zhang[a,1], Honggen Peng[a,*], Xiaojuan You[a], Cheng Peng[a], Xianglan Xu[a], Wenming Liu[a], Xiuzhong Fang[a], Zheng Wang[b], Ning Zhang[a], Xiang Wang[a]

[a] Institute of Applied Chemistry, College of Chemistry, Nanchang University, Nanchang, Jiangxi 330031, China
[b] State Key Laboratory of High-Efficiency Utilization of Coal & Green Chemical Engineering, Ningxia University, Yinchuan 750021, China
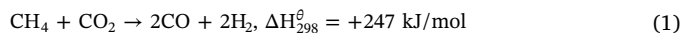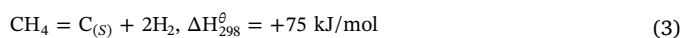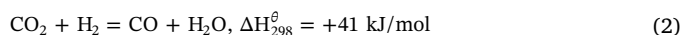
ABSTRACT

Dry reforming of methane (DRM) is a fascinating reaction that utilizes two greenhouse gases (CH_4 and CO_2) to produce value-added synthesis gas (syngas, a mixture of CO and H_2) or hydrogen as a green energy source. Ni-based nanomaterials are considered the most promising DRM catalysts used in industry. However, Ni-based catalysts have sintering and stability problems that need to be resolved. Herein, Ni nanoparticles (NPs) confined in mesopores of aluminum-modified SBA-15 (AlSBA-15) were prepared for the first time using ethylene glycol (EG) as the solvent and delivery conveyor (Ni/AlSBA-15-EG). Transmission electron microscopy (TEM) and high-angle annular dark-field scanning transmission electron microscopy (HAADF-STEM) results showed that ultra-small Ni NPs (average particle size, 3.1 nm) were successfully embedded into the hexagonal mesopores of AlSBA-15 with a perfect peasecod-like structure. Compared with Ni/SBA-15-EG, the Ni/AlSBA-15-EG catalyst exhibited better catalytic activity and coke resistance in DRM. To further test their hydrothermal stability under more harsh reaction conditions (the reverse water gas shift reaction takes place under DRM conditions), the catalysts were first tested in the methane steam reforming reaction. After testing for 20 h, the Ni/AlSBA-15-EG catalyst retained its original structure, while the mesopores of Ni/SBA-15-EG had totally collapsed. This clearly indicated that the Ni/AlSBA-15-EG catalyst had superior hydrothermal stability and potential for long-term use in the DRM reaction (in which the reverse water gas shift reaction is present). Therefore, the ultra-small Ni particle size, confinement effect deriving from the mesoporous channels of AlSBA-15 support, and superior hydrothermal stability (derived from Al-stabilized SBA-15) are proposed as the main factors contributing to the excellent performance of Ni/AlSBA-15-EG catalyst in methane reforming reactions. This strategy could be used to design other high-performance Ni-based catalysts for DRM.

1. Introduction

With increasing global CO_2 emissions year on year, the resultant "greenhouse effect" is causing rising global temperatures and significant climate change [1–4]. As an important research area in energy and environmental science, the chemical conversion of CO_2 into value-added chemicals is a pivotal step toward C—C cycling and reducing the atmospheric CO_2 concentration [2,5]. Dry reforming of methane (DRM) is a promising approach to CO_2 utilization that can efficiently convert two greenhouse gases (CO_2 and CH_4) into syngas (CO and H_2) [6–8]. The overall DRM reaction is shown in Eq. (1).

$$CH_4 + CO_2 \rightarrow 2CO + 2H_2, \Delta H^{\theta}_{298} = +247 \text{ kJ/mol} \tag{1}$$

Eq. (1) implies that the DRM reaction produces syngas with a H_2/CO molar ratio of 1. However, the reaction is simultaneously accompanied by the reverse water-gas shift (RWGS) reaction (Eq. (2)) and CH_4 decomposition (Eq. (3)), leading to the H_2/CO molar ratio deviating from 1.

$$CO_2 + H_2 = CO + H_2O, \Delta H^{\theta}_{298} = +41 \text{ kJ/mol} \tag{2}$$

$$CH_4 = C_{(S)} + 2H_2, \Delta H^{\theta}_{298} = +75 \text{ kJ/mol} \tag{3}$$

The high price and scarcity of noble metals has restricted their large-scale industrial application, despite their superior catalytic

---

* Corresponding author.
E-mail address: penghonggen@ncu.edu.cn (H. Peng).
[1] These authors contributed equally to this work.

performance and coke resistance [9]. Alternatively, Ni-based catalysts have been extensively investigated for DRM owing to their high initial activity, affluent resource, and low cost [10]. However, under harsh reaction conditions, Ni-based catalysts undergo rapid deactivation due to severe coke deposition and sintering of active Ni NPs [11]. Furthermore, water species are present in the DRM process due to the RWGS reaction, meaning that the hydrothermal stability of catalysts is crucial. Therefore, from both an academic and industrial perspective, improving the coking and sintering resistance, and hydrothermal stability of Ni-based catalysts is highly desirable [12].

Ni particle size is an important factor in the activity and decoking ability of Ni-based catalysts in methane reforming reactions [13]. Generally, smaller Ni particles give catalysts with better activity and coke resistance [14–18]. Therefore, numerous approaches to preventing catalyst deactivation in the DRM by controlling the size and distribution of Ni NPs have been explored [19,20]. Well-ordered mesoporous materials are good candidates for Ni NP supports when preparing catalysts for DRM because the channel confinement effect of mesoporous materials can hinder Ni particle sintering and, consequently, improve the catalyst stability [21–24]. For instance, Chu et al. found that catalytic stability and coke resistance could be improved by the confinement effect of ordered mesopores on well-dispersed Ni NPs [25,26]. Furthermore, Kleitz et al. found that a nanostructured Ni/La_2O_3 catalyst derived from mesoporous $LaNiO_3$ using SBA-15, a form of mesoporous silica, as a hard template showed improved performance due to the confinement effect and high dispersion [27]. By studying monolithic catalysts derived from in-situ supported hydrotalcite-like films on aluminum wires, Zhang et al. found that hierarchical porous structure contributed to their high resistance to coke formation and sintering [6]. Furthermore, Sun et al. found that the mesoporous structure of the M-NCaZr catalyst stabilized Ni NPs *via* the confinement effect, which critical to the high stability of this catalyst in DRM [28]. Recently, our group proposed that an ordered mesoporous structure is favorable for hindering the aggregation of the Ni sites and a critical factor accounting for remarkable reaction performance [29].

The investigation of silica-based mesoporous materials with stable controlled channels is motivated by their large surface area, tunable pore size, and excellent thermal stability [19,30–32]. Royer et al. found that nanoscale nickel oxide containing lanthanum-doped mesoporous silica composite (20LaNiSBA(10)) exhibited superior reaction performance to bulk Ni/La_2O_3 catalyst due to the confinement effect of the mesoporous support [33]. Yang et al. studied MCM-41-supported Ni-based bimetallic catalysts and proposed that the formation of well-dispersed Ni particles was responsible for the high stability of the Ni-Zr-MCM-41 catalyst for DRM [34]. When investigating a ceria-promoted Ni/SBA-15 catalyst, Gong et al. found that the nickel particle growth could be restricted by confinement of the SBA-15 support under harsh reaction conditions [35]. Yang et al. [36] studied the Ni/SBA-15 catalyst for DRM and found that highly dispersed Ni NPs could be obtained from the confinement effect of the SBA-15 pore walls. Zhang et al. also found that the confinement effect derived from the mesoporous channels of the silica support contributed to the enhanced coking and sintering resistance of the Ce-Ni/SBA-15 catalyst for DRM [19].

However, the Ni precursor cannot be effectively delivered into the mesoporous channels using a traditional incipient wetness route with aqueous solution as the solvent, which results in a catalyst that cannot exhibit good catalytic performance while achieving simultaneous coke suppression and sintering resistance. Recently, organic solvents have been used as dispersants and stabilizing agents for metal NPs [14,37–40]. Zhang et al. found that Ni/SBA-15 catalyst prepared using ethylene glycol (EG) as solvent and new delivery conveyor exhibited better coking and sintering resistances in DRM than Ni/SBA-15 prepared using a traditional incipient wetness route due to the smaller Ni particle size and better location of Ni nanoparticles. However, the hydrothermal stability of SBA-15 is poor, which makes it unsuitable for DRM due to the presence of the reverse water gas shift (RWGS;

$CO_2 + H_2 \rightleftharpoons CO + H_2O$) as a side reaction [41]. Zhao et al. systematically studied the hydrothermal stability of a series of AlSBA-15 materials with Si/Al ratios of 10–50 under 100% steam at high temperature (600–800 °C) and found that AlSBA-15 was more hydrothermally stable than pristine pure silica SBA-15 under 100% steam [41,42].

Herein, with the aim of improving the hydrothermal stability and reaction performance of the Ni/SBA-15 catalyst in DRM, ordered mesoporous aluminosilicate (AlSBA-15) catalyst containing a small amount of Al was fabricated and used as a Ni support in the preparation of a DRM catalyst for the first time using EG as solvent and delivery conveyor. All catalysts were also tested in the methane steam reforming reaction to determine their hydrothermal stability under severe reaction conditions.

2. Experimental

2.1. Catalyst preparation

2.1.1. Synthesis of SBA-15 and AlSBA-15 supports

SBA-15 was prepared using Pluronic P123 as the structure-directing agent according to a previous report with minor modifications [43]. Typically, Pluronic P123 (10 g) and concentrated hydrochloric acid (62.57 g) were added to deionized water (319 g). After stirring for about 1 h at 35 °C, a clear solution was obtained. Next, tetraethyl orthosilicate (TEOS, 20.8 g) was added and the solution was stirred for 24 h at 35 °C. The obtained solution was then transferred into a Teflon-lined sealed stainless-steel autoclave and maintained at 100 °C for another 24 h. The solid products were collected by filtration, washed several times with water, and dried overnight at 110 °C. Finally, the obtained solids were calcined at 550 °C for 6 h using a ramping rate of 10 °C/min to remove the template and obtain the final SBA-15 support.

The above procedure was also used to prepare Al-modified SBA-15 (AlSBA-15) using minor modifications. Typically, Pluronic P123 (10 g) and concentrated hydrochloric acid (62.57 g) were added to deionized water (319 g). After stirring for about 1 h at 35 °C, a clear solution was obtained. Next, TEOS (20.8 g) and $NaAlO_2$ (0.4 g) were added and the solution was stirred for 24 h at 35 °C. The obtained solution was then transferred into a Teflon-lined sealed stainless-steel autoclave and maintained at 100 °C for a further 24 h. The solid products were collected by filtration, washed several times with water, and dried overnight at 110 °C. Finally, the obtained solids were calcined at 550 °C for 6 h using a ramping rate of 10 °C/min to remove the template and obtain the final AlSBA-15 support.

2.1.2. Catalyst preparation

The SBA-15 and AlSBA-15 supports prepared above were impregnated with $Ni(NO_3)_2$ solution using EG as solvent and delivery conveyor. After impregnation, the samples were stirred under ambient conditions for 12 h, dried at 80 °C under vacuum, and calcined at 550 °C for 4 h in an air atmosphere to obtain the final Ni/SBA-15-EG and Ni/AlSBA-15-EG catalysts (Ni content was about 7 wt.%, as confirmed by the ICP results in Table S1). For comparison, the above procedure was also used to prepare a Ni/SBA-15-H_2O catalyst by replacing EG with deionized water. As confirmed by the ICP results in Table S1, the atomic Si/Al ratio in the freshly prepared Ni/AlSBA-15-EG catalyst was 21.1, which within experimental error of the initial calculated value (20.5) used for sample preparation.

2.2. Catalyst characterization

X-ray diffraction (XRD) patterns were obtained using a Bruker AXS D8Focus diffractometer equipped with a Cu target and Kα-ray irradiation operating at 40 kV and 30 mA. The 2θ range of 10–90° was scanned with a step of 2° min^{-1} to analyze the crystalline phase type and crystallite size of the samples. Small-angle XRD patterns were collected in the range of 2θ = 0.5–5° to investigate the mesoporous structure of

the catalysts. The calculated experimental error for 2θ of the diffraction peaks was $\pm 0.01°$.

Nitrogen adsorption–desorption analysis was performed at liquid N_2 temperature (77 K) using a Micromeritics ASAP2020. BET (Brunauer–Emmett–Teller) and BJH (Barrett–Joyner–Halenda) methods were used to calculate the specific surface areas and pore size distributions of the samples, respectively.

Hydrogen temperature-programmed reduction (H_2-TPR) measurements were performed using a FINESORB 3010C instrument equipped with a thermal conductivity detector (TCD). The catalysts (50 mg) were pretreated at 120 °C with N_2 flow. After cooling to room temperature, a 30 mL min 10% H_2/Ar gas mixture flow was introduced and H_2-TPR experiments were performed from room temperature to 800 °C with a ramping rate of 10 °C/min. H_2 consumption was quantified using CuO (99.99%) as the calibration standard sample.

Thermogravimetric analysis differential scanning calorimetry (TGA-DSC) was used to analyze the amount of carbon deposition on the spent catalysts. Measurements were performed under an oxidative atmosphere on TAQ600 instrument using a high purity air flow (20 mL/min) from room temperature to 800 °C with a ramping rate of 10 °C/min.

Scanning electron microscopy (SEM) images of the catalysts were collected using a Hitachi S-4800 instrument. Transmission electron microscopy (TEM) images of the catalysts were collected using a Tecnai F30 transmission electron microscope. Scanning transmission electron microscopy (STEM) images of selected samples were recorded using a Tecnai F30 instrument equipped with an energy dispersive spectroscopy (EDS) detector.

The elemental content of the catalysts was determined using inductively coupled plasma–atomic emission spectrometry (ICP-AES) on a Varian 715-ES spectrometer.

2.3. Catalyst activity evaluation

2.3.1. Dry reforming of methane (DRM)

The catalytic performance of the catalysts was evaluated under atmospheric pressure in a fixed-bed microreactor (ID = 6 mm). Typically, sieved catalyst particles (0.1 g, 0.3–0.4 mm) were loaded into the reactor and reduced *in situ* under H_2/Ar at 600 °C for 2 h. A mixed gas flow (volume ratio of CH_4 to CO_2 = 1:1, without any balance gas) with a flow rate of 30 mL min^{-1} was then introduced into the catalyst bed, with the weight hourly space velocity (WHSV) fixed at 18,000 mL g_{cat}^{-1} h^{-1}. Notably, for reaction performance tests at various WHSVs, the gas flow rates were 30, 60, and 120 mL min^{-1}, producing corresponding fixed WHSVs of 18,000, 36,000, and 72,000 mL g_{cat}^{-1} h^{-1}, respectively. To monitor the actual amounts of H_2, CO, CH_4, and CO_2, the outlet gas mixture was analyzed using a GC7900 gas chromatograph equipped with a TCD detector and a TDX-01 column using high purity Ar as the carrier gas. Activity data was collected every 50 °C from 600 °C to 800 °C and the durability test was performed at 700 °C. Based on Eqs. (1)–(7) were used to quantify the conversions of CH_4 (X_{CH_4}) and CO_2 (X_{CO_2}), the molar ratio of H_2 to CO ($R_{H_2/CO}$), and the selectivity for H_2 (S_{H_2}), respectively.

$$X_{CH_4} = \frac{F_{CH_4,in} - F_{CH_4,out}}{F_{CH_4,in}} \times 100\% \tag{4}$$

$$X_{CO_2} = \frac{F_{CO_2,in} - F_{CO_2,out}}{F_{CO_2,in}} \times 100\% \tag{5}$$

$$R_{H_2/CO} = F_{H_2,out}/F_{CO,out} \tag{6}$$

$$S_{H_2} = \frac{F_{H_2}}{2 \times (F_{CH_4,in} - F_{CH_4,out})} \tag{7}$$

2.3.2. Hydrothermal stability test

The hydrothermal stability of the catalysts was test using the steam reforming of methane (SRM). The SRM reaction was carried out under ambient pressure in a quartz tube reactor (quartz tube inner diameter, 6 mm). Typically, sieved catalyst particles (0.4 g, 0.3–0.4 mm) were loaded into the reactor and reduced *in situ* under H_2/Ar at 600 °C for 2 h. The evaporated water steam was obtained by pumping deionized water with a flow rate of 0.064 mL min^{-1} into a heated chamber controlled at 200 °C. Next, evaporated water and CH_4 (40 mL min^{-1}, 99.99%) flows were mixed in a gas mixer before entering the catalyst bed, resulting in a WHSV of 18,000 mL h^{-1} g_{cat}^{-1}. After condensing the excess water using a cold water trap, the amount of formed H_2, CO, and CO_2, and remaining CH_4 in the outlet gas was analyzed on-line by a GC9310 gas chromatograph equipped with a TDX-01 column and TCD detector using high purity Ar as the carrier gas. It should be mentioned here that, for steam reforming of methane, CO and CO_2 can be considered as the converted CH_4 because CH_4 is the only carbon source. In addition, carbon deposition, another possible by-products containing carbon, is not serious due to the existence of superfluous water. Furthermore, the flow rate of CH_4 in the outlet gas for SRM may not be able to be calculated accurately because a small amount of water vapor may also exist in the outlet gas though the excess water was condensed by a cold water trap. Therefore, the CH_4 conversion (X_{CH4}) was calculated using the follow equation:

$$C_{CH_4} = \frac{n_{CO,out} + n_{CO_2,out}}{n_{CH_4,out} + n_{CO,out} + n_{CO_2,out}} \times 100\% \tag{8}$$

3. Results and discussion

3.1. Catalyst performance in the dry reforming of methane

To examine the catalytic performance of the Ni/AlSBA-15-EG, Ni/SBA-15-EG, and Ni/SBA-15-H_2O catalysts, they were subjected to DRM tests at 700 °C for 20 h. The results are shown in Fig. 1. While Ni/SBA-15-H_2O and Ni/SBA-15-EG showed a similar reaction performance initially (Fig. 1(A) and (B)), both the CH_4 and CO_2 conversions using Ni/SBA-15-H_2O decreased gradually with time on stream, indicating that catalyst stability was improved by using ethylene glycol (EG) as the solvent and new delivery conveyor. Ni/AlSBA-15-EG was more stable than Ni/SBA-15-EG, which indicated that the addition of Al improved the performance of Ni/SBA-15-EG. Furthermore, the catalytic activity of Ni/AlSBA-15-EG was in good agreement with the thermodynamic equilibrium data at the corresponding temperature. Notably, the thermodynamic equilibrium data for DRM at different temperatures were calculated assuming that only H_2, CO, and H_2O formation occur.

The H_2/CO ratios and H_2 selectivity of the catalysts are presented in Fig. 1(C) and (D), respectively. The H_2/CO ratio and H_2 selectivity of Ni/AlSBA-15-EG were very stable, while those of Ni/SBA-15-EG decreased slightly with time on stream, perhaps due to an increase in the reverse water-gas shift reaction ($CO_2 + H_2 = CO + H_2O$). This indicated that the reverse water-gas shift (RWGS) side reaction could be suppressed by adding Al to the Ni/SBA-15-EG catalyst. Compared with the Ni/SBA-15-H_2O catalyst, the H_2/CO ratio and H_2 selectivity of the Ni/SBA-15-EG catalyst were more stable with time on stream, demonstrating that using ethylene glycol (EG) as solvent during the impregnation step improved the stability of the Ni/SBA-15 catalyst. Notably, the H_2/CO ratios of all catalysts were a little higher than the thermodynamic equilibrium H_2/CO ratio. This could be due to the thermodynamic equilibrium data of DRM being calculated assuming only H_2, CO, and H_2O formation occurred, while ignoring that carbon might also be present, which could lead to an increase in the H_2/CO ratio [44].

To investigate further, additional tests at different temperatures and higher WHSVs were conducted to determine the beneficial effect of Al modification, with the results shown in Fig. S1. The Ni/AlSBA-15-EG catalyst demonstrated higher catalytic activity than the Ni/SBA-15-EG samples, with the difference becoming larger with increasing WHSV. This further demonstrated that the addition of a small amount of Al
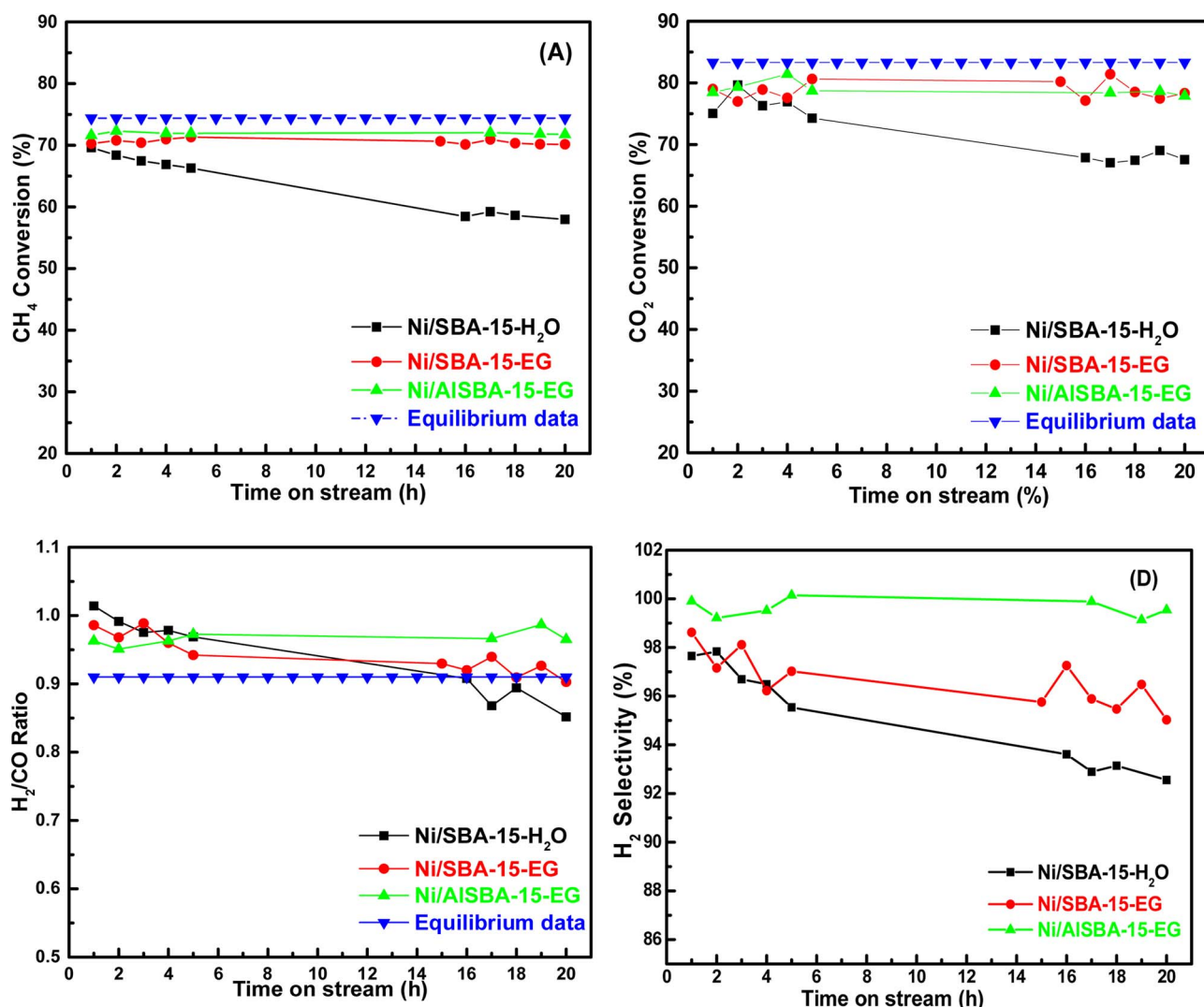
Fig. 1. Durability test of catalysts for DRM at 700 °C for 20 h. (A) methane conversion, (B) CO_2 conversion, (C) H_2/CO ratio, (D) H_2 selectivity. WHSV: 18,000 mL $g_{cat.}^{-1} h^{-1}$, $CH_4/CO_2 = 1$.

improved the reaction performance of the Ni/SBA-15-EG catalyst. Notably, the CH_4 and CO_2 conversions of the Ni/AlSBA-15-EG catalyst were still very close to the thermodynamic equilibrium data at the corresponding temperature, even under more severe reaction conditions, indicating that the catalyst exhibited excellent reaction performance in DRM.

3.2. Catalyst characterization

To clarify the coking properties of the spent catalysts, all three catalysts were analyzed by TGA-DSC after 20 h stability tests, with the results shown in Fig. 2. A small weight gain stage was observed for all catalysts in the temperature range 300–500 °C due to reoxidation of the metallic Ni active species. The Ni/SBA-15-H_2O catalyst showed an evident weight loss stage of about 32.4% at a higher temperature, accompanied by an obvious exothermal peak in the corresponding DSC profiles (Fig. 2(B)), which can be attributed to the combustion of a large amount of formed carbonaceous deposits. Only a very small amount of coke was formed on the surfaces of Ni/SBA-15-EG and Ni/AlSBA-15-EG catalysts under the same conditions, demonstrating that these catalysts possessed better coke resistance than Ni/SBA-15-H_2O prepared using H_2O as solvent. For the Ni/AlSBA-15-EG catalysts, the weight loss was just 1.5%, accompanied by a small exothermal peak in the corresponding DSC profile (Fig. 2(B)), while for Ni/SBA-15-EG the weight

loss was higher, at 3.1%, accompanied by an evident exothermal peak in the corresponding DSC profile (Fig. 2(B)). This result demonstrated that a catalyst with improved coking resistance was obtained by introducing a small amount of Al into the structure of SBA-15 and using EG as precipitation solvent and delivery conveyor.

SEM was used to further investigate coke formation on the surface of all catalysts, with the resultant images shown in Fig. 3. The surfaces of all freshly reduced catalysts were very clean. As shown in Fig. 3(d) and (f), after the stability test for 20 h, no obvious change had occurred to the Ni/SBA-15-EG and Ni/AlSBA-15-EG catalysts, except for slight aggregation. However, a large amount of whisker-like carbon fiber was clearly observed on the Ni/SBA-15-H_2O catalyst. Therefore, SEM results provided additional evidence that the coking resistance was improved by adding a small amount of Al to the structure of SBA-15 and using ethylene glycol (EG) as solvent and delivery conveyor.

To understand the different catalyst performances, N_2 adsorption–desorption isotherms were measured to investigate the textural properties of the catalysts. The adsorption–desorption isotherms and pore size distribution curves of the supports and corresponding freshly reduced catalysts are presented in Fig. S2 and 4, respectively. As shown in Fig. S2, typical type-IV hysteresis loop isotherms with H_1 hysteresis loops were observed for the SBA-15 and AlSBA-15 supports, indicating that uniform tubular pore channels were present in the two supports. Notably, no significant change was observed after the
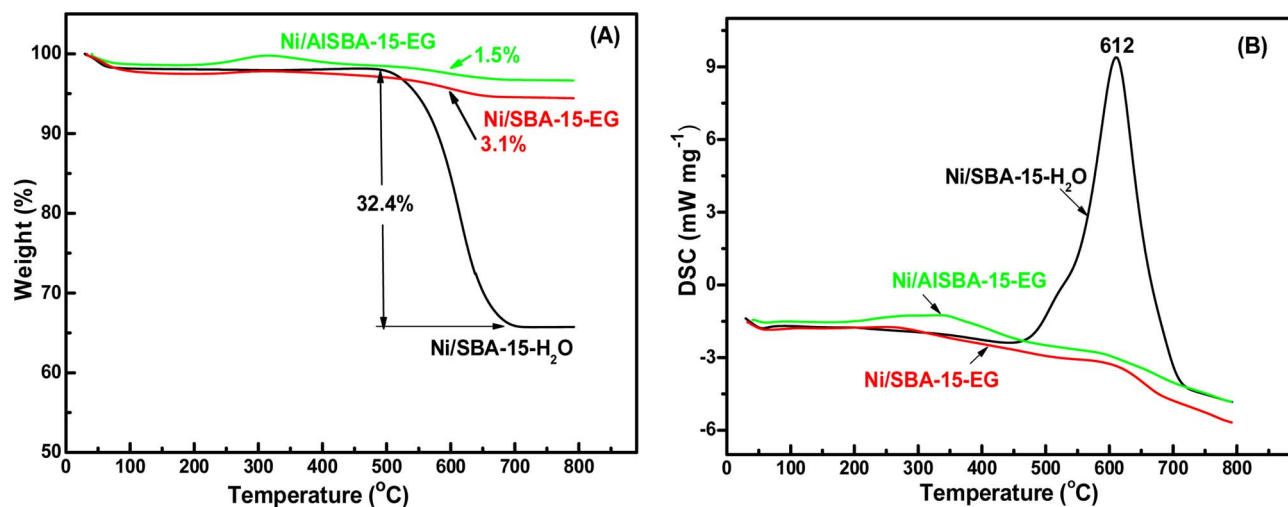
Fig. 2. TGA-DSC profiles of the catalysts after dry reforming of methane at 700 °C for 20 h: (A) TGA; (B) DSC.
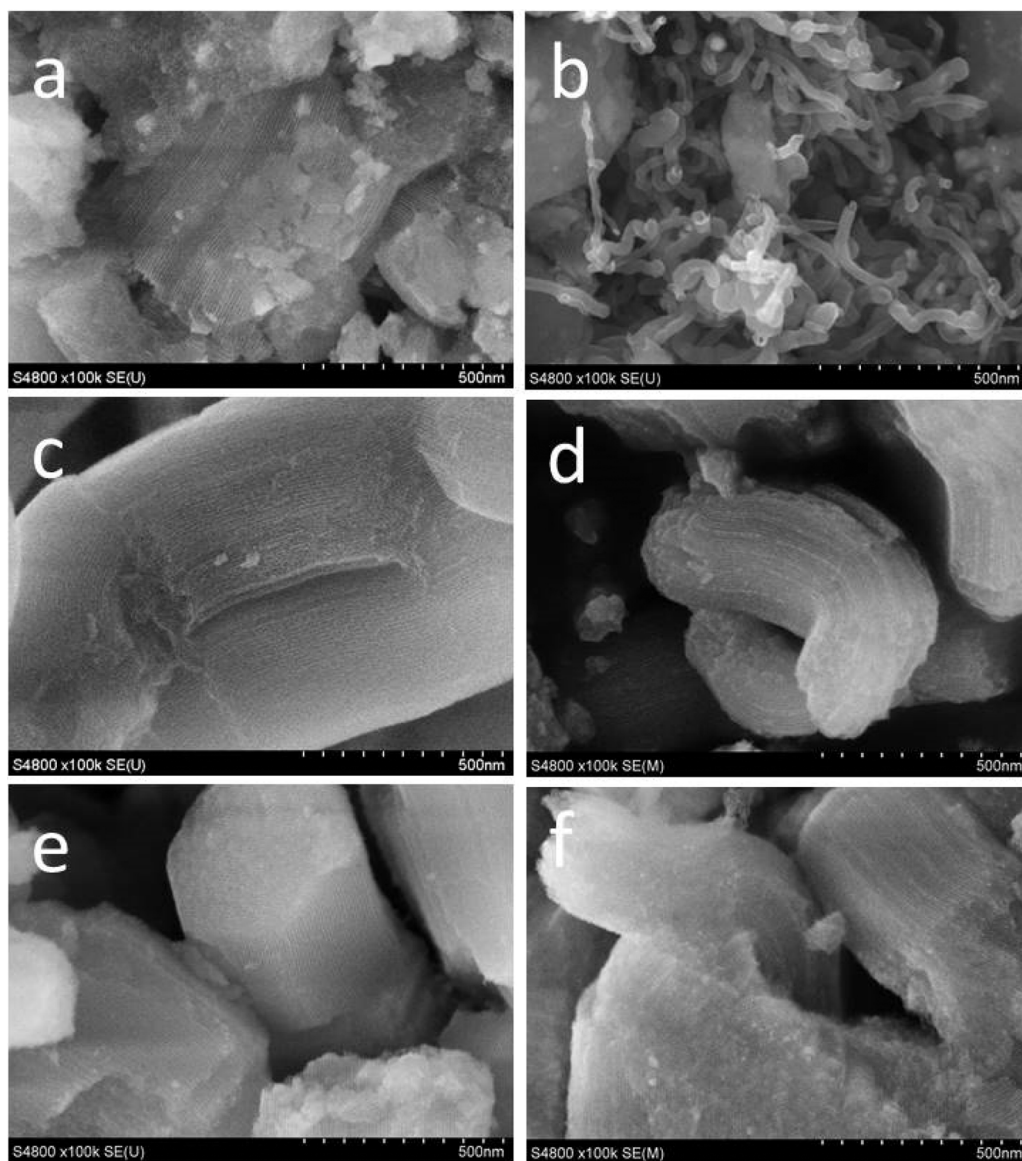

Fig. 3. SEM images of the fresh (left) and spent (right) catalysts: (a, b) Ni/SBA-15-H_2O, (c, d) Ni/SBA-15-EG and (e, f) Ni/AlSBA-15-EG.
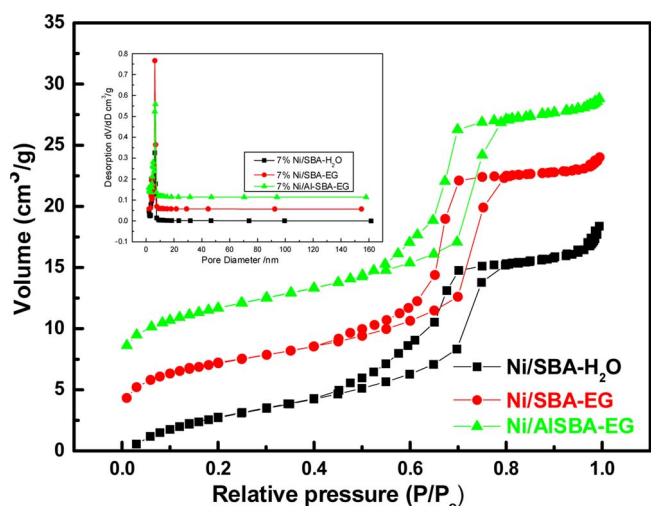
Fig. 4. N_2 adsorption-desorption isotherms and pore size distribution profiles (inset) of the freshly reduced catalysts.

Table 1
Physico-chemical properties of the freshly reduced catalysts and supports.

Catalysts	S_{BET} (m^2 g^{-1})	Pore size (nm)	Pore volume (cm^3 g^{-1})
SBA-15	654	8.6	1.38
AlSBA-15	688	6.5	1.15
Ni/SBA-15-H$_2$O	604	5.7	0.80
Ni/SBA-15-EG	558	6.2	0.86
Ni/AlSBA-15-EG	567	6.5	0.87

introduction of a small amount of Al in SBA-15 (AlSBA-15) compared with the SBA-15 sample, indicating that Al addition had no significant impact on the support structure. As shown in Fig. 4, the freshly reduced catalysts showed no significant difference in the N_2 adsorption–desorption isotherms, which indicated that the mesoporous structures were retained after Ni impregnation. For comparison, the textural properties of all samples are summarized in Table 1. Slight decreases in BET surface area, pore size, and pore volume were observed after Ni impregnation, indicating that the Ni particles had successfully entered the pore systems or blocked the pore entrances of the supports.

To clarify the catalyst phase compositions, XRD patterns were recorded, as shown in Fig. 5. Typical diffraction peaks of Ni crystallites

Table 2
Crystallite sizes of the freshly reduced and spent catalysts.

Catalysts	Ni crystallite size[a] (nm)	
	Reduced catalysts	Spent catalysts
Ni/SBA-15-H$_2$O	15.6	24.2
Ni/SBA-15-EG	3.6	5.2
Ni/AlSBA-15-EG	3.2	4.6

were observed in all of the freshly reduced catalysts (Fig. 5(A)). However, the widths at half height of the Ni crystallite peak on different supports varied, which indicated that the supported Ni species had different crystallinities. For comparison, the Ni crystallite sizes of the freshly reduce catalysts were calculated and are shown in Table 2. The Ni crystallite sizes of the catalysts were in the order Ni/SBA-15-H$_2$O > Ni/SBA-15-EG $\approx$ Ni/AlSBA-15-EG. This result was consistent with TEM characterization. In general, catalysts with smaller Ni crystallite sizes exhibit better activity and coke resistance [14–17,45]. The relatively small Ni crystallite size of the Ni/SBA-15-EG and Ni/AlSBA-15-EG catalysts was beneficial to their excellent reaction performance in the DRM. Notably, the Ni crystallite size of the Ni/SBA-15-H$_2$O catalyst (15.6 nm) was larger than the pore size of the corresponding SBA-15 support (8.6 nm), which further confirmed that most Ni particles were not confined into the channels of SBA-15 using H$_2$O for delivery. Furthermore, as shown in Table 2, the Ni crystallite size of the Ni/SBA-15-H$_2$O catalyst increased from an initial 15.6 nm to 24.2 nm after the 20-h stability test, which was much larger than that of the other two catalysts. The large Ni crystallite sizes and lack of confinement for most Ni particles were likely responsible for the lower stability and coke resistance of Ni/SBA-15-H$_2$O among the catalysts tested. Furthermore, a new graphite peak was observed on the Ni/SBA-15-H$_2$O and Ni/SBA-15-EG catalysts after the 20-h stability test, which reflected that these two catalysts underwent more severe coking than the Ni/AlSBA-15-EG catalyst.

The TEM technique was used to determine the morphologies, Ni particle sizes, and particle size distributions of the freshly reduced catalysts, with the results shown in Fig. 6. For the Ni/SBA-15-H$_2$O catalyst, a large number of Ni NPs were attached on the external surface of SBA-15 with a size distribution ranging from 5.3 nm to 52 nm, with a mean size of about 16.2 nm (Fig. 6(A)). The mean particle size of the Ni NPs was much bigger than the pore diameter of the SBA-15 support (8.6 nm), which further demonstrated that most Ni NPs had not embedded in the channels of SBA-15 using H$_2$O as solvent. The lack of the confinement effect deriving from the support for most Ni particles was
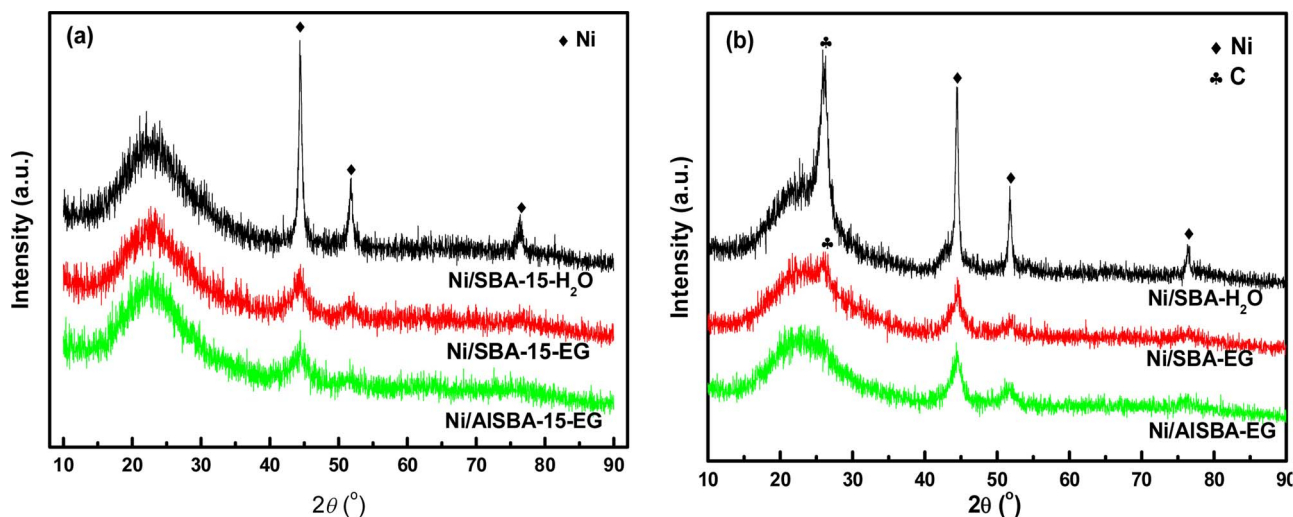

Fig. 5. Wide angle XRD patterns of the freshly reduced (a) and spent (b) catalysts.
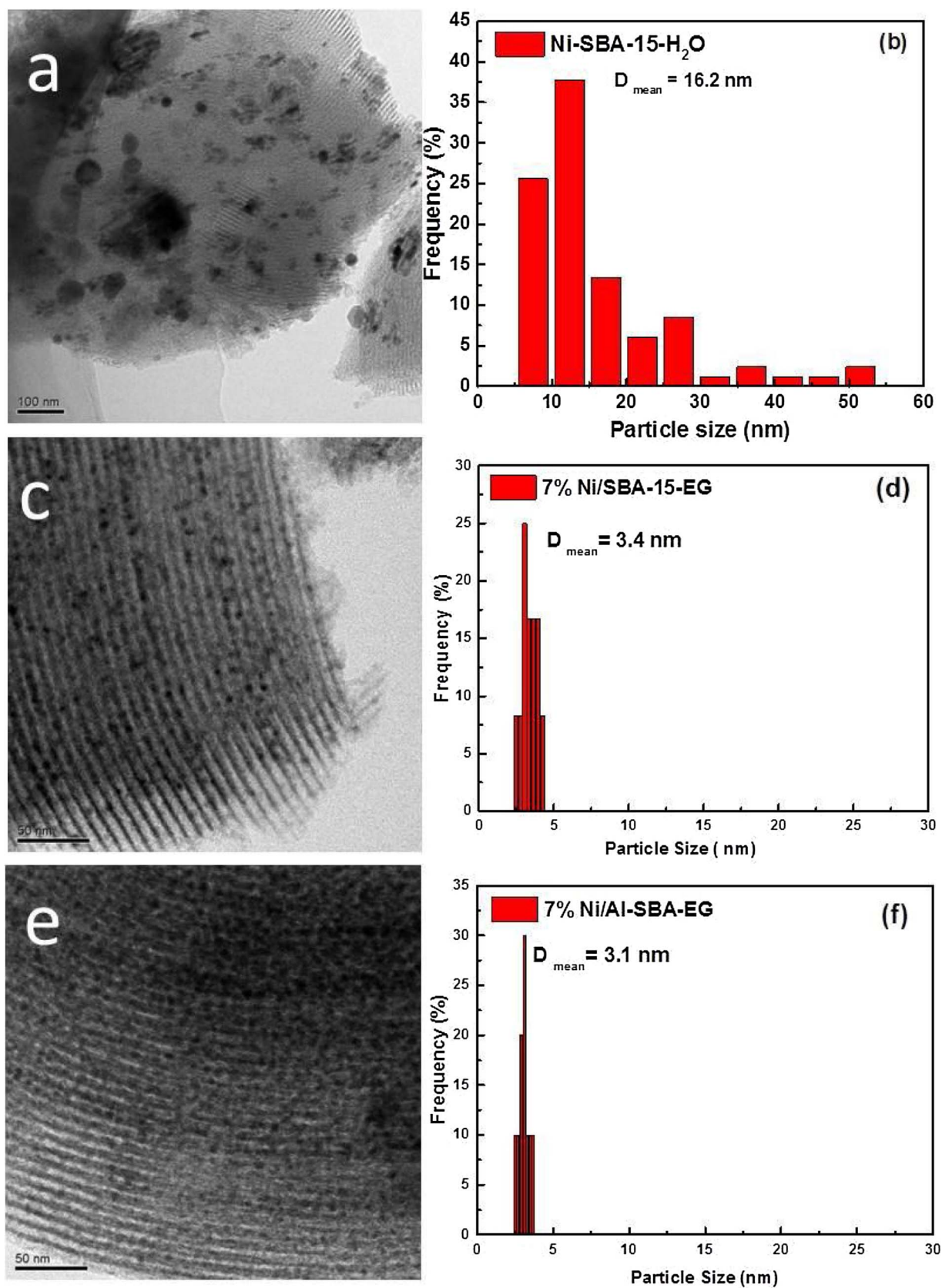
Fig. 6. TEM images (left) and Ni particles size distribution (right) of the freshly reduced catalysts: (a, b) Ni/SBA-15-H₂O (c, d), Ni/SBA-15-EG and (e, f) Ni/AlSBA-15-EG.
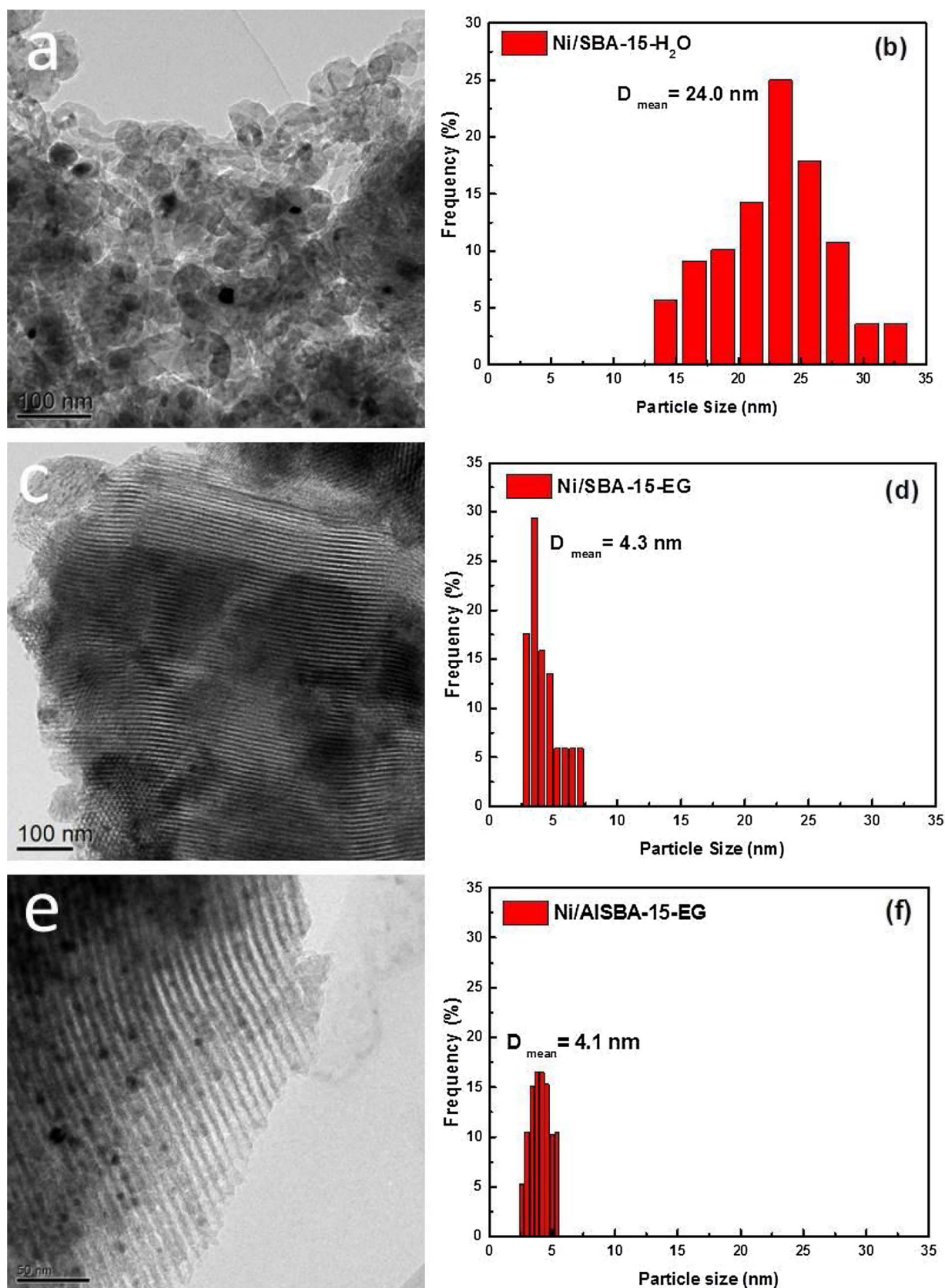
Fig. 7. TEM images (left) and Ni particles size distribution (right) of the spent catalysts: (a, b). Ni/SBA-15-H$_2$O, (c, d) Ni/SBA-15-EG, and (e, f) Ni/AlSBA-15-EG.

likely responsible for the lower reaction performance and coking resistance of the Ni/SBA-15-H_2O catalyst among the catalysts tested. For the Ni/SBA-15-EG catalyst, almost all small particles were distributed between the observed stripes, indicating that most Ni particles were anchored into the ordered mesoporous channels using EG as the precipitation solvent. This efficiently prevented particle sintering and coke deposition because most Ni particles were restricted to the mesoporous channels of SBA-15 and AlSBA-15. The TEM image and Ni particle size distribution of the Ni/AlSBA-15-EG catalyst were very similar to those of the Ni/SBA-15-EG catalyst, with a tiny particle size and uniform distribution of Ni NPs observed. This meant that the Al-modified SBA-15 had no negative effect on Ni NPs trapped in the channels. Furthermore, the Ni particle size of the freshly reduced Ni/SBA-15-EG and Ni/AlSBA-15-EG catalysts was only about 3 nm. It has been previously reported that Ni particle size plays a pivotal role in coke resistance and reforming activity, with catalysts with smaller Ni particle sizes exhibiting better activity and coke resistance [14–17]. In particular, if the Ni particles were smaller than 5 nm, carbon deposition can be significantly suppressed [16,46]. Notably, compared with Ni/SBA-15-H_2O catalyst, the relatively small Ni particle size of the Ni/SBA-15-EG and Ni/AlSBA-15-EG catalysts could play an important role in their excellent reaction performance and superior coke resistance.

For comparison, the catalysts used in DRM for 20 h were also analyzed by TEM, as shown in Fig. 7. No significant change occurred to any of the catalysts, except for a collapse of the ordered mesoporous structure in the Ni/SBA-15-H_2O catalyst, which indicated that this
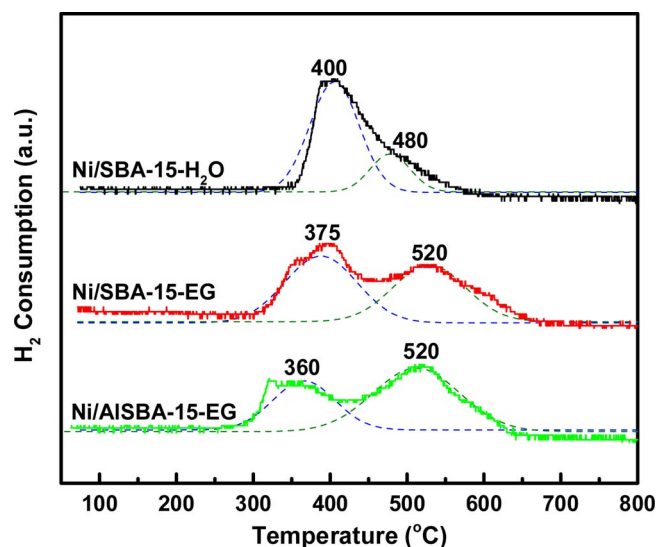

Fig. 9. H_2-TPR profiles of the freshly calcined catalysts.

catalyst did not survive under DRM conditions. In contrast, the TEM images of the Ni/SBA-15-EG and Ni/AlSBA-15-EG catalysts (Fig. 7(c) and (e)) showed that the ordered mesoporous structure was preserved. Furthermore, the particle sizes of Ni/SBA-15-EG and Ni/AlSBA-15-EG
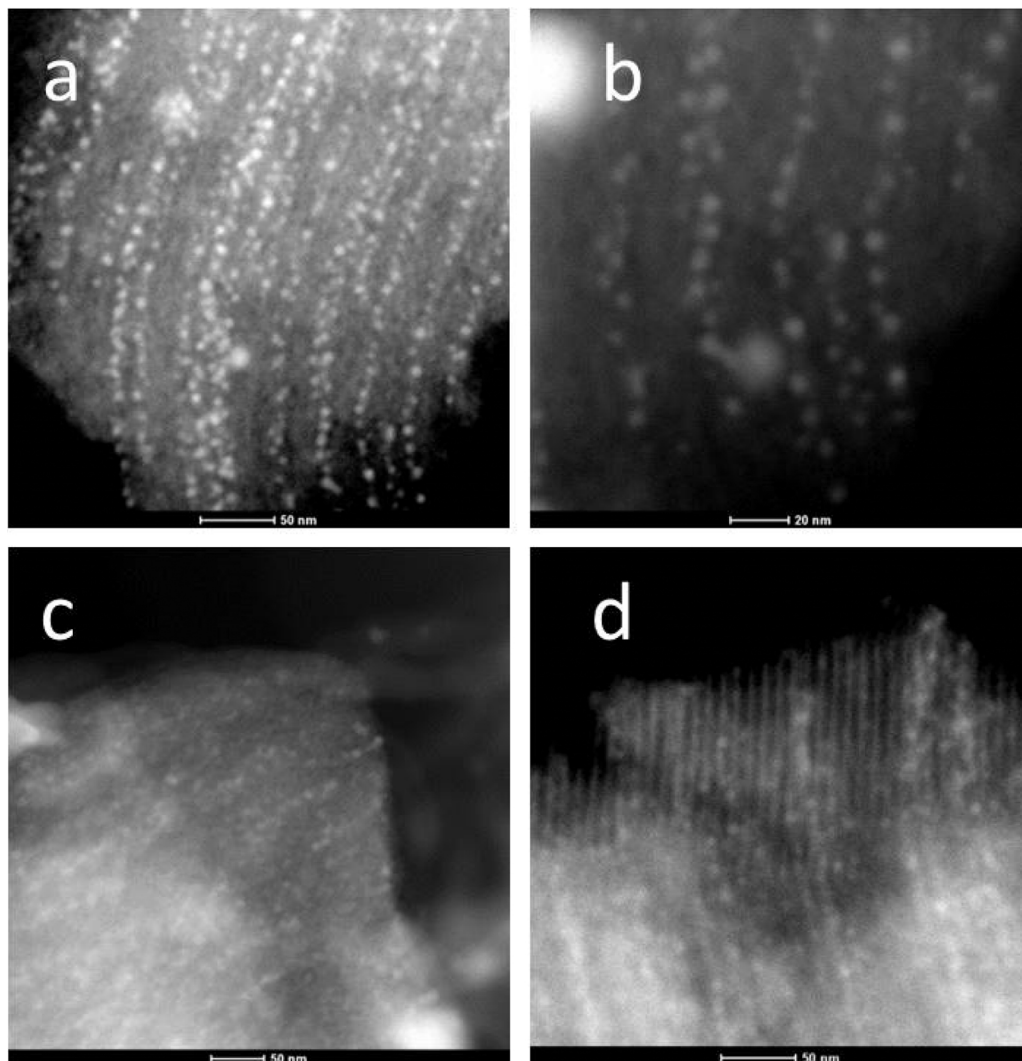

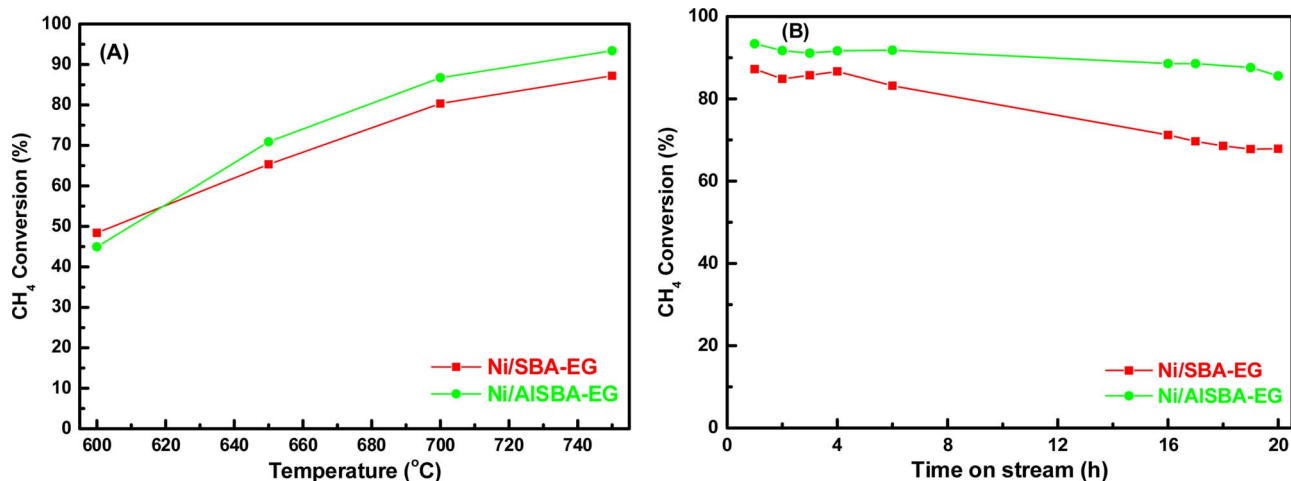Fig. 8. HAADF-STEM images of the freshly reduced (a, b) and spent (c, d) Ni/AlSBA-15-EG catalyst.

Fig. 10. Reaction performance of Ni/SBA-15-EG and Ni/AlSBA-15-EG catalysts for steam reforming of methane: (A) catalytic activity; (B) catalytic stability.
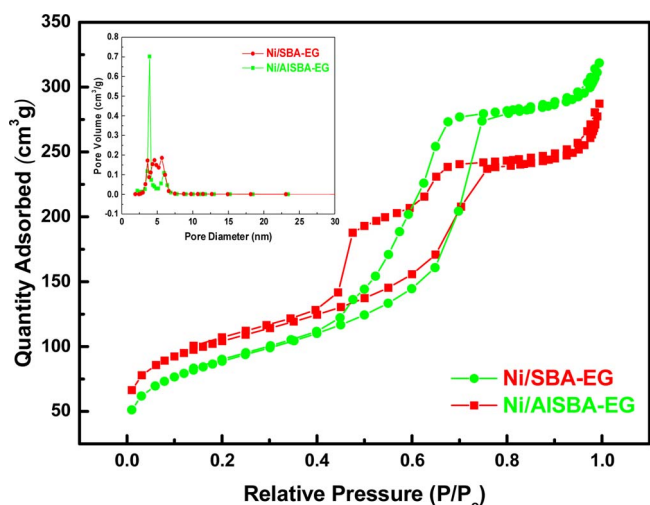

Fig. 11. N_2 adsorption-desorption isotherms and pore size distribution curves (inset) of Ni/SBA-15-EG and Ni/AlSBA-15-EG after methane stem reforming.

Table 3
Texture structure of the Ni/SBA-15-EG and Ni/AlSBA-15-EG catalysts before and after methane stem reforming.

Catalysts	S_{BET} (m²/g)		Pore size (nm)		Pore volume (cm³/g)	
	fresh	spent	fresh	spent	fresh	spent
Ni/SBA-15-EG	558	314	6.5	5.3	0.87	0.51
Ni/AlSBA-15-EG	567	361	6.2	4.9	0.86	0.47

catalysts used for 20 h were similar to those of the freshly reduced catalysts (Fig. 6(c) and (e)), which indicated that no significant aggregation occurred on the Ni particles. However, the Ni particle size of the Ni/SBA-15-H_2O catalyst increased from the initial 16.2 nm to 24.0 nm, which was much larger than that of the other catalysts under the same conditions. This clearly showed that the metallic Ni species was less stable on the Ni/SBA-15-H_2O catalyst. Therefore, it was reasonable to deduce that the Ni particles were efficiently confined in the channel of the support by using EG as the precipitation solvent and delivery conveyor.

High-angle annular dark field-scanning electron microscopy (HAADF-STEM) was used to further observe Ni NPs embedded in the channels of freshly reduced and spent Ni/AlSBA-15-EG catalyst, as shown in Fig. 8. Highly ordered arrays of Ni particles were embedded in

the ordered mesoporous channels in both the freshly reduced and spent Ni/AlSBA-15-EG catalysts with a perfect peasecod-like structure, which demonstrated that homogeneously dispersed Ni particles were obtained and maintained under the harsh reaction conditions. Therefore, the ultra-small Ni particle size and channel confinement effect of Ni/AlSBA-15-EG catalyst were factors determining its superior reaction performance for DRM.

To investigate the Ni reducibility of the catalysts, all freshly calcined samples underwent H_2-TPR measurements, with the profiles and quantified results shown in Fig. 9 and Table S2, respectively. As shown in Table S2, the H/Ni atomic ratios of all catalysts were around a stoichiometric value of 2, while the H_2 consumption was very close to the theoretical value of 1.19 mmol g_{cat}^{-1} for the complete reduction of Ni^{2+} (7 wt.% on support) to metallic Ni, showing that the valence state of Ni species was $+2$ in all freshly calcined samples. All freshly calcined catalysts gave two reduction peaks, which can be ascribed to the reduction of NiO in different chemical environments to metallic Ni [17,47–49]. In general, the peak around 380 °C can be assigned to the reduction of NiO species with weak contact with the support, while the higher temperature shoulder peak at about 520 °C was attributed to the reduction of NiO species embedded in the mesopores with intimate contact with the support. For a supported catalyst, as reported previously, the sintering resistance and stability of the active metal can be improved by strengthening metal-support interaction [40,50–53]. For better comparison, by deconvoluting the profiles, the molar percentages of the two types of NiO species corresponding to the two reduction peaks were calculated for all catalysts, as shown in Table S2. The molar percentage of the NiO species with intimate contact increased in the order Ni/SBA-15-H_2O < Ni/SBA-15-EG < Ni/AlSBA-15-EG, while that of the NiO species with weak contact decreased in the same order. Therefore, NiO species had the strongest interaction with support in the Ni/AlSBA-15-EG catalyst, resulting in this catalyst showing the best reaction performance.

3.3. Hydrothermal stability test of Ni/Al-SBA-15

The reverse water gas shift (RWGS) side reaction also occurs during in the DRM reaction. Therefore, the hydrothermal stability of the mesoporous silica material support used for DRM should be considered. To our knowledge, there has been no report on the hydrothermal stability of Ni supported on silica catalysts. To quickly evaluate the hydrothermal stability of Ni/AlSBA-15-EG and Ni/SBA-15-EG, the methane steam reforming reaction was used, with the results shown in Fig. 10. The CH_4 conversion of all catalysts increased with increasing reaction temperature due to the strong endothermic effect of methane steam reforming (Fig. 10(A)). In the low temperature region, the Ni/SBA-15-
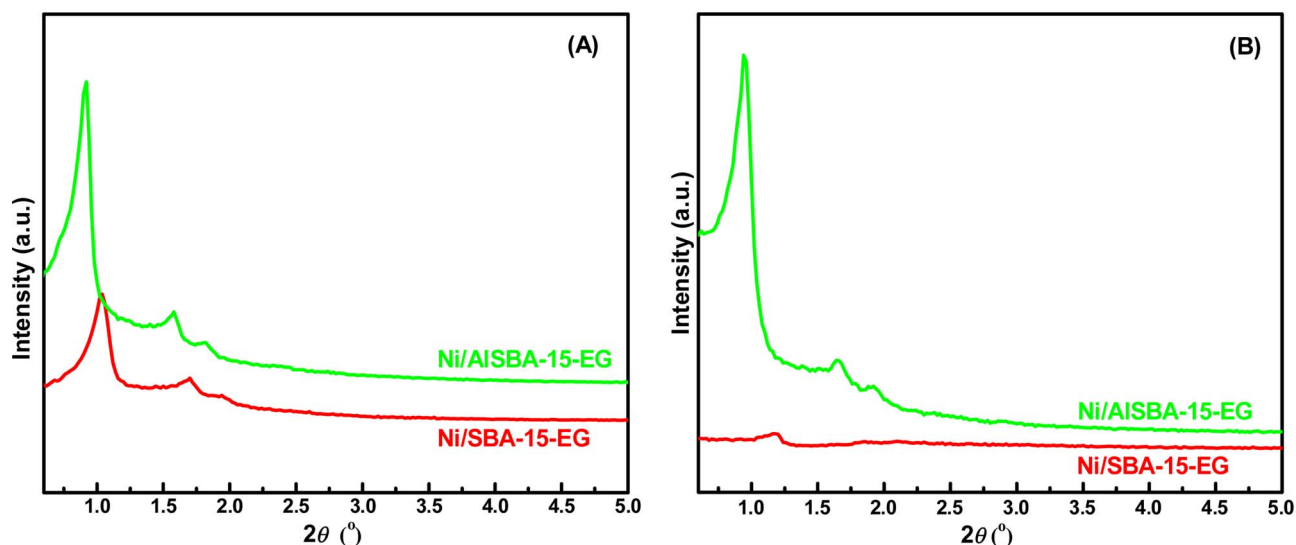
Fig. 12. Small angle XRD patterns of the Ni/SBA-15-EG and Ni/AlSBA-15-EG catalysts: (A) the freshly reduced catalysts; (B) the spent catalysts.

EG and Ni/AlSBA-15-EG catalysts exhibited comparable activity. However, above 650 °C the Ni/AlSBA-15-EG catalyst possessed the higher CH_4 conversion. Furthermore, as shown in Fig. 10(B), the CH_4 conversion of Ni/AlSBA-15-EG decreased more slowly than that of Ni/SBA-15-EG, although they obtained comparable initial CH_4 conversion at 800 °C during the 20-h stability test. This showed that the reaction performance of the Ni/AlSBA-15 catalyst was improved by introducing small amount of Al into the structure of SBA-15.

To further clarify the differences in hydrothermal stability between Ni/SBA-15-EG and Ni/AlSBA-15-EG catalysts, N_2 adsorption–desorption isotherms were recorded for all samples after the 20-h stability test, as shown in Fig. 11. Typical type-IV hysteresis loop isotherms with H_1 hysteresis loops were observed for the spent Ni/AlSBA-15-EG catalyst, reflecting that the mesoporous structure was mostly maintained after the 20-h methane steam reforming stability test. However, for spent Ni/SBA-15-EG catalyst, a relatively wide and distorted hysteresis loop with a wide pore size distribution was obtained, indicating that the mesostructure of this sample was extensively degraded and partially collapsed. For comparison, the textural properties of all the samples are summarized in Table 3. The BET surface area, pore size, and pore volume of the Ni/SBA-15-EG catalysts changed more obviously than those of the Ni/AlSBA-15-EG sample, which further confirmed that the mesostructure of AlSBA-15 was more stable than that of SBA-15.

To further investigate the effect of Al introduction on the hydrothermal stability of SBA-15, the freshly reduced and spent catalysts were analyzed by XRD, with the small-angle XRD patterns shown in Fig. 12. Both freshly reduced Ni/SBA-15-EG and Ni/AlSBA-15-EG catalysts exhibited three well-resolved diffraction peaks belonging to the 100, 110, and 200 reflections of 2-D hexagonal p6 mm symmetry (Fig. 12(A)), which indicated the existence of a highly ordered mesostructure [42]. In comparison, as shown in Fig. 12(B), three well-resolved diffraction peaks belonging to the 100, 110, and 200 planes were also clearly observed on the Ni/AlSBA-15-EG catalyst after the 20-h methane steam reforming stability test, which demonstrated that the highly ordered mesostructure was maintained. However, for the spent Ni/SBA-15-EG catalyst, no diffraction peaks corresponding to the 2-D hexagonal p6 mm symmetry were observed, which demonstrated that the mesostructure had suffered severe degradation and collapse. In summary, the small angle XRD patterns were in good agreement with the N_2 adsorption–desorption results, demonstrating that introducing a small amount of Al significantly improved the hydrothermal stability of Ni/AlSBA-15, which ultimately affected the reaction performance of the catalysts in the methane reforming reactions.

4. Conclusions

In conclusion, a novel catalyst (Ni/AlSBA-15-EG) comprising Ni NPs confined in the mesopores of AlSBA-15 was prepared for the first time using ethylene glycol (EG) as the solvent and delivery conveyor and used in methane reforming reactions. TEM and STEM results showed that Ni particles can be delivered and embedded into the channels of mesoporous silica with a perfect peasecod-like structure. Compared with Ni/SBA-15-EG, the Ni/AlSBA-15-EG catalyst exhibited better catalytic performance and superior hydrothermal stability in methane dry and steam reforming. The ultra-small Ni particle size, confinement effect deriving from the mesoporous channels of the AlSBA-15 support, and superior hydrothermal stability derived from the Al stabilized SBA-15 were likely the main factors contributing to the excellent catalyst performance of Ni/AlSBA-15-EG. This strategy can be used to design other high performance Ni-based catalysts for DRM.

Appendix A. Supplementary data

Supplementary data associated with this article can be found, in the online version, at http://dx.doi.org/10.1016/j.apcatb.2017.11.001.

References

[1] W. Wang, S. Wang, X. Ma, J. Gong, Chem. Soc. Rev. 40 (2011) 3703–3727.
[2] S. Kawi, Y. Kathiraser, Front. Energy Res. 3 (2015) 1–17.
[3] J.-P. Zou, D.-D. Wu, J. Luo, Q.-J. Xing, X.-B. Luo, W.-H. Dong, S.-L. Luo, H.-M. Du, S.L. Suib, ACS Catal. 6 (2016) 6861–6867.
[4] W.-H. Dong, D.-D. Wu, J.-M. Luo, Q.-J. Xing, H. Liu, J.-P. Zou, X.-B. Luo, X.-B. Min, H.-L. Liu, S.-L. Luo, C.-T. Au, J. Catal. 349 (2017) 218–225.
[5] L. Shi, G. Yang, K. Tao, Y. Yoneyama, Y. Tan, N. Tsubakl, Acc. Chem. Res. 46 (2013) 1838–1847.
[6] X. Du, D. Zhang, L. Shi, R. Gao, J. Zhang, Nanoscale 5 (2013) 2659–2663.
[7] M.S. Challiwala, M.M. Ghouri, P. Linke, M.M. El-Halwagi, N.O. Elbashir, J. CO₂ Util. 17 (2017) 99–111.
[8] W. Taifan, J. Baltrusaitis, Appl. Catal. B 198 (2016) 525–547.
[9] J. Liu, H. Peng, W. Liu, X. Xu, X. Wang, C. Li, W. Zhou, P. Yuan, X. Chen, W. Zhang,

H. Zhan, ChemCatChem 6 (2014) 2095–2104.

[10] X. Li, D. Li, H. Tian, L. Zeng, Z.-J. Zhao, J. Gong, Appl. Catal. B 202 (2017) 683–694.

[11] X. Fang, J. Lian, K. Nie, X. Zhang, Y. Dai, X. Xu, X. Wang, W. Liu, C. Li, W. Zhou, J. Energy Chem. 25 (2016) 825–831.

[12] X. Zhao, H. Li, J. Zhang, L. Shi, D. Zhang, Int. J. Hydrogen Energy 41 (2016) 2447–2456.

[13] R. Dębek, M. Motak, M.E. Galvez, T. Grzybek, P. Da Costa, Appl. Catal. B (2017), http://dx.doi.org/10.1016/j.apcatb.2017.06.024.

[14] T. Xie, L. Shi, J. Zhang, D. Zhang, Chem. Commun. 50 (2014) 7250–7253.

[15] H. Peng, X. Zhang, L. Zhang, C. Rao, J. Lian, W. Liu, J. Ying, G. Zhang, Z. Wang, N. Zhang, X. Wang, ChemCatChem 9 (2017) 127–136.

[16] H.S. Bengaard, J.K. Nørskov, J. Sehested, B.S. Clausen, L.P. Nielsen, A.M. Molenbroek, J.R. Rostrup-Nielsen, J. Catal. 209 (2002) 365–384.

[17] Y. Zhang, W. Wang, Z. Wang, X. Zhou, Z. Wang, C.-J. Liu, Catal. Today 256 (2015) 130–136.

[18] Z. Shang, S. Li, L. Li, G. Liu, X. Liang, Appl. Catal. B 201 (2017) 302–309.

[19] T. Xie, X. Zhao, J. Zhang, L. Shi, D. Zhang, Int. J. Hydrogen Energy 40 (2015) 9685–9695.

[20] Z. Li, M. Li, Z. Bian, Y. Kathiraser, S. Kawi, Appl. Catal. B 188 (2016) 324–341.

[21] L. Xu, Z. Miao, H. Song, W. Chen, L. Chou, Catal. Sci. Technol. 4 (2014) 1759–1770.

[22] H. Ma, L. Zeng, H. Tian, D. Li, X. Wang, X. Li, J. Gong, Appl. Catal. B 181 (2016) 321–331.

[23] K. Jabbour, P. Massiani, A. Davidson, S. Casale, N. El Hassan, Appl. Catal. B 201 (2017) 527–542.

[24] A. Ungureanu, B. Dragoi, A. Chirieac, S. Royer, D. Duprez, E. Dumitriu, J. Mater. Chem. 21 (2011) 12529–12541.

[25] N. Wang, K. Shen, L. Huang, X. Yu, W. Qian, W. Chu, ACS Catal. 3 (2013) 1638–1651.

[26] N. Wang, Z. Xu, J. Deng, K. Shen, X. Yu, W. Qian, W. Chu, F. Wei, ChemCatChem 6 (2014) 1470–1480.

[27] M.M. Nair, S. Kaliaguine, F. Kleitz, ACS Catal. 4 (2014) 3837–3846.

[28] N. Sun, X. Wen, F. Wang, W. Wei, Y. Sun, Energy Environ. Sci. 3 (2010) 366–369.

[29] X. Fang, C. Peng, H. Peng, W. Liu, X. Xu, X. Wang, C. Li, W. Zhou, ChemCatChem 7 (2015) 3753–3762.

[30] M. Wang, Q. Zhang, T. Zhang, Y. Wang, J. Wang, K. Long, Z. Song, X. Liu, P. Ning, Chem. Eng. J. 313 (2017) 1370–1381.

[31] Q. Wei, G. Yang, X. Gao, N. Yamane, P. Zhang, G. Liu, N. Tsubaki, Chem. Eng. J. 327 (2017) 465–473.

[32] B. Dragoi, A. Ungureanu, C. Ciotonea, A. Chirieac, S. Petit, S. Royer, E. Dumitriu,

[33] J.P. Dacquin, D. Sellam, C. Batiot-Dupeyrat, A. Tougerti, D. Duprez, S. Royer, ChemSusChem 7 (2014) 631–637.

[34] D. Liu, X.Y. Quek, W.N.E. Cheo, R. Lau, A. Borgna, Y. Yang, J. Catal. 266 (2009) 380–390.

[35] D. Li, L. Zeng, X. Li, X. Wang, H. Ma, S. Assabumrungrat, J. Gong, Appl. Catal. B 176–177 (2015) 532–541.

[36] W. Yang, D. He, Appl. Catal. A 524 (2016) 94–104.

[37] W. Zhan, Q. He, X. Liu, Y. Guo, Y. Wang, L. Wang, Y. Guo, A.Y. Borisevich, J. Zhang, G. Lu, S. Dai, J. Am. Chem. Soc. 138 (2016) 16130–16139.

[38] W. Zhan, Y. Shu, Y. Sheng, H. Zhu, Y. Guo, L. Wang, Y. Guo, J. Zhang, G. Lu, S. Dai, Angew. Chem. Int. Ed. 56 (2017) 4494–4498.

[39] M.N. Kaydouh, N. El Hassan, A. Davidson, S. Casale, H. El Zakhem, P. Massiani, Microporous Mesoporous Mater. 220 (2016) 99–109.

[40] W. Zhan, Q. He, X. Liu, Y. Guo, Y. Wang, L. Wang, Y. Guo, A.Y. Borisevich, J. Zhang, G. Lu, S. Dai, J. Am. Chem. Soc. 138 (2016) 16130–16139.

[41] C. Xia, B.S. Liu, Y.H. Guo, Ind. Eng. Chem. Res. 53 (2014) 2189–2196.

[42] Q. Li, Z. Wu, B. Tu, S.S. Park, C.-S. Ha, D. Zhao, Microporous Mesoporous Mater. 135 (2010) 95–104.

[43] D. Zhao, Q. Huo, J. Feng, B.F. Chmelk, G.D. Stucky, J. Am. Chem. Soc. 120 (1998) 6024–6036.

[44] D. Pakhare, J. Spivey, Chem. Soc. Rev. 43 (2014) 7813–7837.

[45] J.W. Han, J.S. Park, M.S. Choi, H. Lee, Appl. Catal. B 203 (2017) 625–632.

[46] W. Chen, G. Zhao, Q. Xue, L. Chen, Y. Lu, Appl. Catal. B 136–137 (2013) 260–268.

[47] R.K. Singha, A. Shukla, A. Yadav, L.N. Sivakumar Konathala, R. Bal, Appl. Catal. B 202 (2017) 473–488.

[48] X. Fang, X. Zhang, Y. Guo, M. Chen, W. Liu, X. Xu, H. Peng, Z. Gao, X. Wang, C. Li, Int. J. Hydrogen Energy 41 (2016) 11141–11153.

[49] U. Oemar, M.L. Ang, Y.C. Chin, K. Hidajat, S. Kawi, Catal. Sci. Technol. 5 (2015) 3585–3597.

[50] X. Zhang, X. Fang, X. Feng, X. Li, W. Liu, X. Xu, N. Zhang, Z. Gao, X. Wang, W. Zhou, Catal. Sci. Technol. 7 (2017) 2729–2743.

[51] Q. Xin, A. Papavasilou, N. Boukos, A. Glisenti, J.P.H. Li, Y. Yang, C.J. Philippopoulos, E. Poulakis, F.K. Katsaros, V. Meynen, P. Cool, Appl. Catal. B (2017), http://dx.doi.org/10.1016/j.apcatb.2017.03.071.

[52] F. Wang, L. Xu, J. Zhang, Y. Zhao, H. Li, H.X. Li, K. Wu, G.Q. Xu, W. Chen, Appl. Catal. B 180 (2016) 511–520.

[53] S. Dama, S.R. Ghodke, R. Bobade, H.R. Gurav, S. Chilukuri, Appl. Catal. B (2017), http://dx.doi.org/10.1016/j.apcatb.2017.10.048.